Journal of
Composites Science

MDPI

Article

Inline Profiling of Reactive Thermoplastic Pultruded GFRP Rebars: A Study on the Influencing Factors

Moritz Fünkner [1,*], Georg Zeeb [1,2], Michael Wilhelm [1], Peter Eyerer [1] and Frank Henning [1,2]

[1] Department of Polymer Engineering, Fraunhofer Institute for Chemical Technology (ICT), Joseph-von-Fraunhofer Straße 7, 76327 Pfinztal, Germany; georg.zeeb@ict.fraunhofer.de (G.Z.); michael.wilhelm@ict.fraunhofer.de (M.W.); peter.eyerer@ict.fraunhofer.de (P.E.); frank.henning@ict.fraunhofer.de (F.H.)
[2] Institute of Vehicle Systems Technology (FAST)—Lightweight Engineering, Karlsruhe Institute of Technology (KIT), Rintheimer Querallee 2, 76131 Karlsruhe, Germany
* Correspondence: moritz.fuenkner@ict.fraunhofer.de; Tel.: +49-7214640670

Abstract

Compared to reinforcing concrete with steel bars, rebars—made of fiber-reinforced plastic—have a high potential for resource savings in the construction industry due to their corrosion resistance. For the large-volume market of reinforcement elements, efficient manufacturing processes must be developed to ensure the best possible bond behavior between concrete and rebar. In contrast to established FRP-rebars made with thermosetting materials, the use of a thermoplastic matrix enables surface profiling without severing the edge fibers as well as subsequent bending of the bar. The rebars to be produced in this study are based on the process of reactive thermoplastic pultrusion of continuously glass fiber reinforced aPA6. Their surface must enable a mechanical interlocking between the reinforcement bar and concrete. Concepts for a profiling device have been methodically developed and evaluated. The resulting concept of a double wheel embossing unit with a variable infeed and an infrared preheating section is built as a prototype, implemented in a pultrusion line, and further optimized. For a comprehensive understanding of the embossing process, reinforcement bars are manufactured, characterized, and evaluated under parameter variation according to a statistical experimental plan. The present study demonstrates the relationship between the infeed, preheating temperature, and haul-off speed with respect to the embossing depth, which is equivalent to the rib height. No degradation of the Young's modulus was observed as a result of the profiling process.

Keywords: pultrusion; glass fiber; thermoplastic; polyamide 6; profiling; rebar; construction

Academic Editor: Peng Zhang

Received: 2 December 2025
Revised: 10 January 2026
Accepted: 14 January 2026
Published: 19 January 2026

1. Introduction

Concrete is produced on a vast scale, and the cement used in it accounts for roughly 7–8% of global CO_2 emissions [1,2]. Consequently, strategies that increase material efficiency in reinforced concrete and extend service life are particularly impactful in lowering greenhouse gas emissions. Beyond conventional steel reinforcement, Fiber-Reinforced Polymer (FRP) systems and textile reinforcements have emerged as promising alternatives, enabling thinner, lighter structural elements while maintaining durability and performance [3]. Adoption of FRP reinforcements is growing rapidly in regions with high durability demands, such as North America and Asia [4].

Steel reinforcement requires adequate concrete cover to limit corrosion in aggressive environments. Electrochemical corrosion of steel is one of the primary constraints to

structural durability in reinforced concrete, leading to increased maintenance efforts and cover thicknesses dictated by durability rather than strength requirements. FRP rebars, in contrast, do not undergo electrochemical corrosion and have shown favorable durability in moist concrete and chloride exposures [5]. This corrosion resistance has the potential to reduce the need for maintenance-intensive concrete structures, optimize material volumes, and achieve resource savings.

Reliable bonding between reinforcement and concrete is critical to transferring forces effectively, ensuring durability, and realizing material savings. In FRP-reinforced concrete, bonding relies predominantly on mechanical interlocking from surface profiles, as chemical adhesion is limited between FRP materials and concrete [6,7]. Common profiling approaches include milled helical grooves, sand coatings, and tightly wrapped helical rovings, as shown in Figure 1.

Figure 1. Overview of differently profiled rebars. From left to right: FRP-rebars with a milled helical groove, FRP-rebar with sand coating, FRP-rebars with a tight helical roving wrapping, conventional steel rebar.

The governing failure mode depends mainly on concrete strength: in low-strength concrete, crushing of the concrete ribs or shear failure of the winding tends to dominate, whereas in higher-strength concretes and Ultra-High-Performance-Concrete (UHPC), shear failure of the FRP ribs or wrapped rovings becomes dominant [8,9]. Increasing rib height generally improves bond, but the effect is degressive. Achillides and Pilakoutas observed limited additional gains and a shift in failure mechanisms beyond moderate deformation heights [7].

Most commercially available FRP rebars are based on thermoset matrices (e.g., vinyl ester, epoxy) cured during pultrusion or similar processes [10]. After cure, thermosets cannot be reshaped, so producing deformations by milling or cutting will sever load-bearing surface fibers, which reduces tensile capacity and stress transfer in the rebars outer regions [6,11].

In contrast, thermoplastic matrices enable local reheating and shaping of surface ribs and allow post-forming (e.g., bending stirrups) without cutting the fibers [12]. As such, thermoplastic FRP rebars present promising solutions for applications that require both enhanced durability and post-forming capabilities. Beyond bond, resource efficiency is affected by how profiling impacts axial properties. Milling grooves removes surface fibers and lowers the utilization of the fiber bundle. Apitz et al. reported a tensile utilization rate of 74.1% for milled grooves versus 87.4% for embossed profiles, underscoring the efficiency potential of deformation-based profiling that avoids fiber cutting [11].

Prior studies have explored several routes to create mechanical interlocking in thermoplastic FRP rebars. Böhm et al. demonstrated offline embossing/pressing of polyamide-based CFRP rods, highlighting that localized heating of the outer layers before pressing is advantageous, but reported limitations in fiber volume fraction and continuity of the process [13]. Schumann et al. integrated surface profiling into the pultrusion line and formed ribs by pressing at an elevated temperature. However, manual application led to

nonuniform rib quality [14]. El-Tahan et al. produced thermoplastic CFRP rebars and stirrups by compression molding and noted undulations in the ribbed surface layer. Applying tension during forming was proposed to mitigate fiber waviness and premature failure under pull-out tests [12].

Taken together, these findings highlight a key design target: maximizing the shear capacity of surface-near FRP ribs while avoiding fiber damage, especially for applications in UHPC where bond demand is high [6,8,9].

Several recent advancements have sought to address these limitations: The study by Wang et al. evaluates mechanical behaviors and bond performance of basalt fiber-reinforced thermoplastic rebars manufactured with different surface features. While showing promising mechanical behavior, ribbed rebars had to be fabricated by manual secondary processing due to manufacturing difficulty [15]. This highlights the need for a scalable inline manufacturing method.

Zeng et al. recently presented a novel inline technique for adding resin bumps on pultruded thermoplastic GFRP bars by wrapping a nylon-mesh, which created gaps for resin bumps on the surface. This technique demonstrates potential for scalability by manufacturing the novel surface features inline [16]. However, the nylon mesh had to be torn off leading to waste and the created ribs were not fiber reinforced, which could potentially be a weak point of the bond interface.

Clark et al. introduced an innovative Continuous Forming Machine for manufacturing thermoplastic composite rebars, focusing on surface profiling to enhance mechanical interlocking with concrete. This study aligns with the current work's goal of leveraging thermoplastic technology to develop inline profiling methods that improve bond behavior and preserve fiber continuity, crucial for structural applications such as UHPC reinforcement [17]. The main difference to this work lies in the raw materials and initial pultrusion process: Clark et al. used pre-impregnated PETG unidirectional tapes which are consolidated to a round bar and achieved a fiber mass fraction of 58%.

Luo et al. and Zeng et al. provided a systematic synthesis of research on thermoplastic FRP composites in construction. Their review highlights the growing relevance and potential of thermoplastic systems in reducing carbon emissions while improving long-term durability. This aligns with the objectives of the present study to advance scalable profiling methods tailored for thermoplastic FRP [18,19].

Reactive thermoplastic processing offers unique advantages for scaling up production of FRP rebars. The polymerization of ε-caprolactam to form anionic polyamide-6 (aPA6) matrices enables continuous manufacturing at high fiber volume fractions with efficient use of process heat [20–22]. Despite significant progress in understanding thermoplastic FRP profiling techniques, gaps remain in developing inline-capable systems that not only preserve surface fiber continuity but also enable predictable rib geometry under controllable manufacturing parameters such as infeed, preheating temperature, and haul-off speed. These relationships are critical for achieving reliable bond performance, as surface deformation geometry and rib height influence bond efficiency significantly.

This study addresses these gaps by designing and implementing a novel double-wheel inline embossing unit with infrared preheating, integrated into a reactive aPA6 pultrusion line. Furthermore, a statistical Design of Experiments (DoE) framework was employed to quantify the parametric effects of infeed, preheating temperature, and haul-off speed on rib height while verifying the preservation of axial stiffness. This process-level advancement complements ongoing efforts to study bond mechanisms and the durability of thermoplastic FRP rebars in applications such as Ultra-High-Performance Concrete (UHPC). Dedicated bond tests are outlined as the next step in fully validating the approach.

2. Materials and Methods

2.1. Materials

The glass fibers utilized were StarRov® PR 440 2400 886 (by Johns Manville, Denver, CO, USA), which are coated with a sizing agent suitable for reactive thermoplastic processing. The aPA6 matrix was formed during the pultrusion process using AP-Nylon® caprolactam flakes, sodium-caprolactamate catalyst (Bruggolen® C10), and hexamethylene-1,6-dicarbamoylcaprolactam (Bruggolen® C20P). All components of the aPA6 matrix were procured from L. Brüggemann GmbH & Co., KG, Heilbronn, Germany.

2.2. Methods for Manufacturing

The pultrusion process is set up according to a known stable processing parameter window with a die for a round bar with a diameter of 20 mm. The bar contained 240 rovings at 2400 tex each. Assuming the density of E-glass ≈ 2.62 g/cm^3 the theoretical fiber volume fraction is ≈70.0%.

The embossing unit is placed in the pultrusion line between the die and the pulling unit after a cooling section of 2800 mm downstream of the die outlet. After the cooling section, the rod should already have cooled down significantly. In the area directly in front of the embossing unit, a heating section of infrared emitters is used to bring the surface area to a targeted temperature. The approach aims to achieve a solid core of the rod while allowing for easier local deformation of the hotter outer layers. A defined rod temperature is set by changing the emitter power. Figure 2 shows a schematic illustration of this experimental setup.

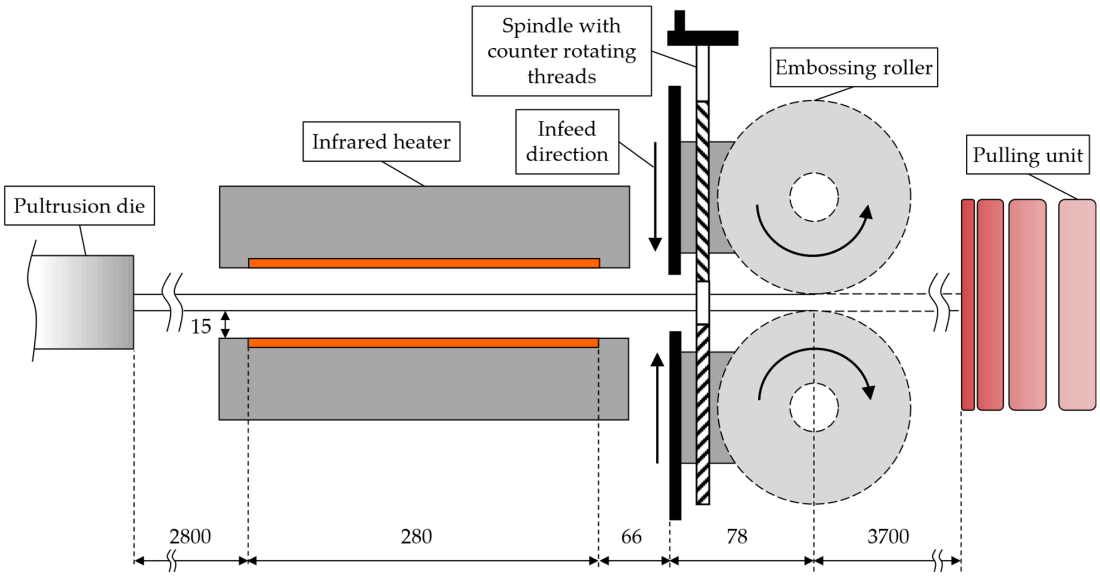

Figure 2. Experimental setup of the embossing unit at the pultrusion line. All dimensions in mm.

The concept for inline profiling chosen and implemented for this study consists of two shaping embossing rollers, each of which is mounted on a linear slide, see Figure 2. A spindle with counter-rotating threads allows the two slides to be moved uniformly towards each other to a defined embossing infeed, thus applying a force to the pultrusion profile. The two rollers roll freely on the rod surface and are not additionally driven.

A compromise had to be made for the positioning of the embossing device between the tool and the pulling unit. A large cooling distance between the pultrusion die (left) and the infrared heater section is advantageous to achieve increased cooling of the core section, but downstream of the embossing device, the profile must be sufficiently cooled down again so that the pulling unit (right) can work safely and without slippage. The distance between the IR section and the embossing device is kept as short as possible (66 mm + 78 mm = 144 mm)

without limiting the possibility of temperature measurement using an IR thermometer. The chosen distance of the infrared emitters to the profile of 15 mm represents a middle ground between transferable thermal power and adjustability of the surface temperature.

At the beginning of each test group, the infeed of the embossing unit is calibrated. A 30 min settling time is implemented after the pultrusion process begins to establish a stable process window. Setting different preheating temperatures requires multiple measurements of the surface temperature and readjustments of the emitter power. At least five reinforcing bars with a length of 2 m were produced for each parameter setpoint. The ambient temperature during experiments was around 23 °C with approx. 33% relative humidity.

Figure 3 shows the profiling device in use during an experiment. The embossing rollers are designed as a three-piece construction with top and bottom guiding plates to center the pultrusion profile in the right height and to allow a profile deformation only where the embossing teeth are. To reduce the temperature of the embossed profile when entering the pulling unit, cooling air is provided by the blue tubes above and below the profile. Figure 4 shows three representative profiled bars produced under distinct process parameter sets from the trial plan (Section 2.3).

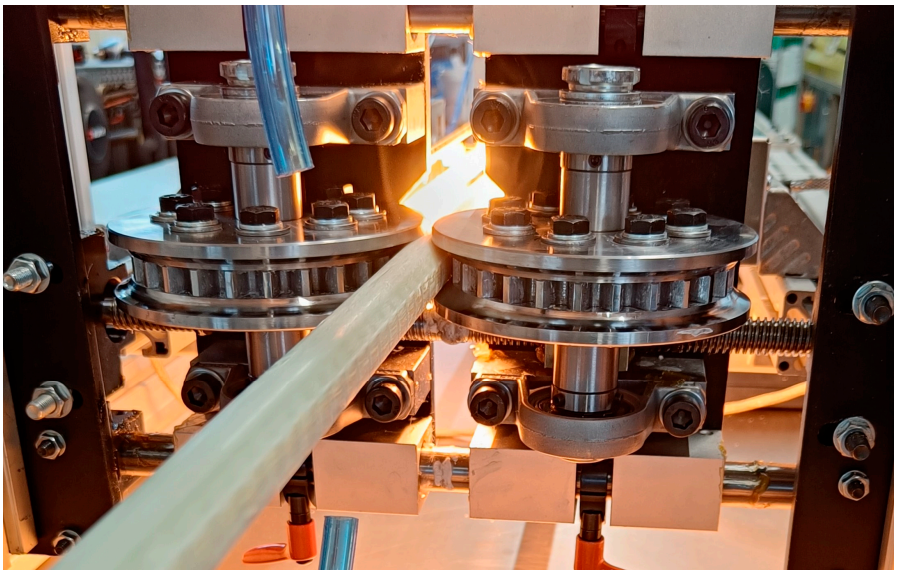

Figure 3. Experimental setup. The Embossing rollers are designed as a three-piece construction with guiding plates. The blue tubes provide cooling air to reduce the temperature of the profile when entering the pulling unit.

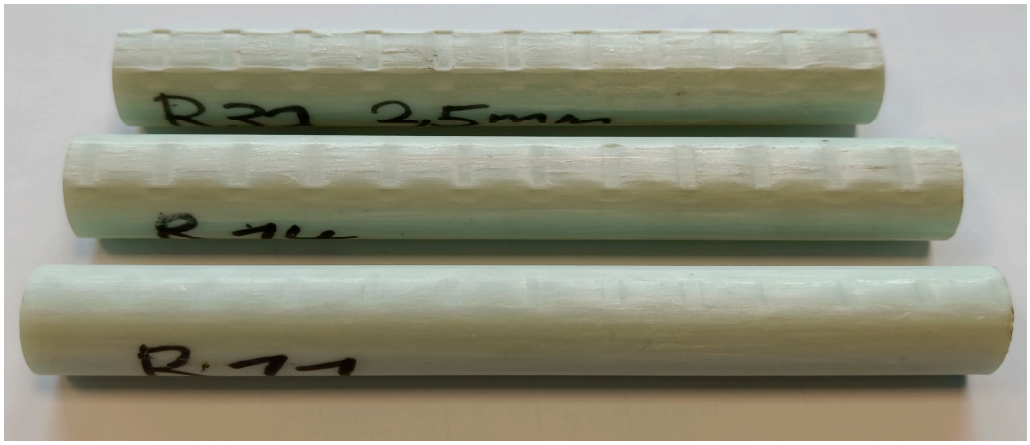

Figure 4. Examples for the profiled bars manufactured with different process parameters. Top to bottom: R32, R14, R11 (see Section 2.3.).

2.3. Design of Experiments

For a basic understanding of the process, it is necessary to identify the parameters relevant to the embossing result first. In the further course of this work, these will be used as factors in a Design of Experiments (DoE) trial campaign. A parameter diagram was created, which is shown in Figure 5. The input and output variables based on the system "Inline profiling in reactive thermoplastic pultrusion" were divided into five different categories: Control parameters, Input parameters, Noise parameters, Intended output and Error states. A detailed explanation of the diagram can be found in the relevant literature [23].

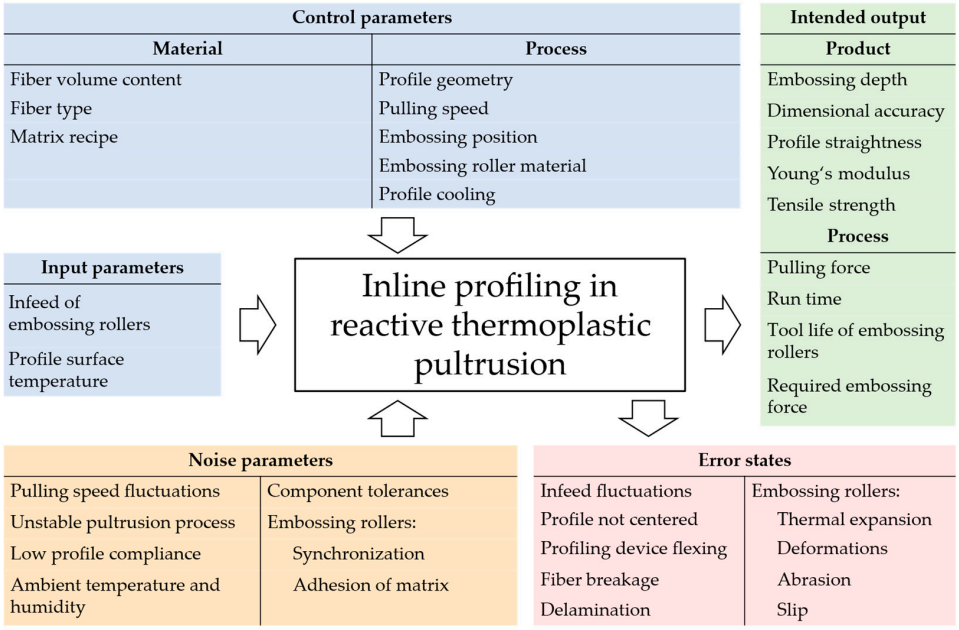

Figure 5. Parameter diagram of the system "Inline profiling in reactive thermoplastic pultrusion".

Based on the parameter diagram, the most promising influencing variables have been identified with the help of preliminary tests and were used as factors for the DoE study carried out. Infeed and haul-off speed have a significant influence on the embossing result. The principle of first cooling the rod and then heating it up in the surface area promises to reduce the necessary embossing forces and improve dimensional precision. Therefore, the preheating temperature of the rod surface is considered as a third factor. The main objective of the profiling method is to enable mechanical interlocking between the reinforcing bar and the concrete. The resulting embossing depth makes the greatest contribution to the transferable forces and therefore forms a target variable to be investigated. In his studies, Niewels demonstrated that a low Young's modulus of the rebars can lead to larger cracks in the reinforced concrete component under load, compared to using conventional steel rebars with a Young's modulus of 210 GPa [24]. Therefore, the Young's modulus of the rebars was chosen as a second target variable, because of its significance in relation to bond behavior and the anticipation of its dependence on the chosen factors.

The systematic planning of this test campaign enables the description of not only linear effects of the influencing variables but also non-linear effects and interactions between them. A central-composite-circumscribed (CCC) design is chosen for this work. This results in five setting levels per factor, which must be reliably adjustable. The infeed levels are determined by the results of preliminary tests and cover the parameter range achieved with the embossing unit during those tests. The melting temperature (T_m) of aPA6 is around 220 °C [25]. This represents the mean setting of the profile temperature before embossing. The low and high settings are selected at 210 °C and 230 °C, respectively, which are both

above and below the melting temperature. This covers both optimization directions and the temperature of 10 K above the melting point, as suggested by Böhm et al. [13] for a similar form pressing process. The selected haul-off speeds reflect stable settings, which were found in the basic process development of pultrusion with ε-caprolactam [21,22]. The trial plan's CCC design requests additional factor settings, called starpoints, which are determined by extending the previously selected low and high settings in their respective directions by a factor of 1.682. Table 1 summarizes the investigated parameters.

Table 1. Parameter range of the factors investigated in the DoE study built on a CCC trial plan.

Parameter	Unit	Starpoint Low	Low Setting	Center Point	High Setting	Starpoint High
Infeed	mm	0.16	0.5	1.0	1.5	1.84
Profile surface temperature	°C	203	210	220	230	237
Haul-off speed	m/min	0.3	0.5	0.8	1.1	1.3

From a statistical point of view, randomization of the experimental sequence is expressly desired. However, the haul-off speed cannot be changed arbitrarily quickly; it requires adjustments in small steps to the desired speed to keep the pultrusion process stable. For this reason, the tests are combined into groups of similar haul-off speeds whenever possible. For each experimental group, the pultrusion process is only started once. The center point, which represents the middle setting of all factors simultaneously, must be repeated three times and is randomly interspersed (R25, R26, R27). In this way, the repeatability of the tests can be evaluated afterwards.

Based on the most promising parameter settings identified during the experiments, two additional tests (R31 and R32) have been added to the trial plan. Additionally, R33 represents the parameter setting for smooth bars without any profiling, serving as a reference. In summary, Table 2 shows the CCC trial plan in the performed order.

Table 2. CCC experimental design of the DoE study performed. Parameter settings of additional tests R31, R32 and smooth bars R33 as reference.

Order of Experiments	Experiment Name	Infeed [mm]	Profile Temperature Before Embossing [°C]	Haul-Off Speed [m/min]
1	R19	0.16	220	0.8
2	R25	1	220	0.8
3	R20	1.84	220	0.8
4	R21	1	203	0.8
5	R26	1	220	0.8
6	R22	1	237	0.8
7	R15	0.5	210	1.1
8	R16	1.5	210	1.1
9	R17	0.5	230	1.1
10	R18	1.5	230	1.1
11	R24	1	220	1.3
12	R27	1	220	0.8
13	R11	0.5	210	0.5
14	R12	1.5	210	0.5
15	R13	0.5	230	0.5
16	R14	1.5	230	0.5
17	R23	1	220	0.3
18 *	R33	-	-	0.8
19	R31	2	230	0.8
20	R32	2.5	230	0.8

* smooth bars as reference.

2.4. Characterization Methods

2.4.1. Measuring the Embossing Depth

To measure the embossing depth, a section of the rod is placed within a 3D-printed semi-circular support (black) that has been designed specifically to fit the diameter of the rod, as can be seen in Figure 6. In the lower area of the semi-circular support, a recess is provided for the profiled surface. This allows the ribs to be tested to be aligned parallel to the reference surface (green line) without the rod being tilted accidentally. The local embossing depth is defined as the difference between h_1 (maximum overall height) and h_2 (minimum overall height). The resulting embossing depth achieved in each experiment is calculated as the average value of five measurements.

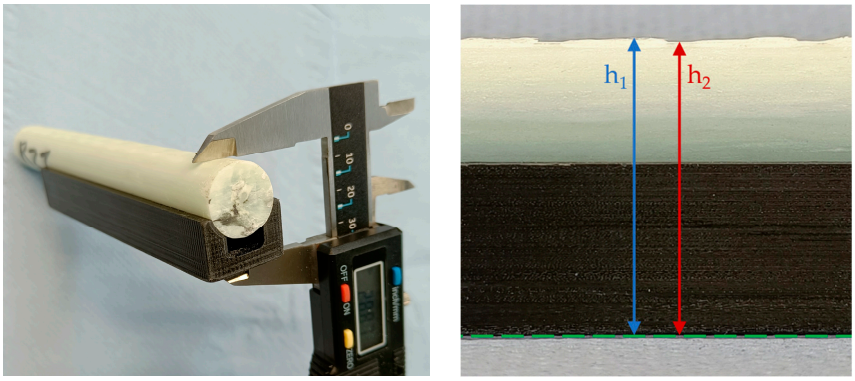

(**a**) (**b**)

Figure 6. (**a**) Semi-circular support (black) with profiled rebar from the DoE study. (**b**) Measuring the embossing depth as the difference between h_1 (maximum height) and h_2 (minimum height) based on a reference surface (green line). Note: localized fiber damage is visible in the outermost surface layers in the macro image Figure 6b. Its exact position along the ribs cannot be unambiguously determined from the macro view. The longitudinal microsection in Section 3.4. is taken exactly through the bar mid-plane and does not intersect these outer regions.

2.4.2. Tensile Tests

The tensile tests conducted in this study adhere to ISO 10406-1 standards, and the experimental setup is illustrated in Figure 7 [26]. The rods were clamped in a way so that there was an identical overhang on both sides. To avoid early failure due to compressive forces in the clamping area, steel tubes (outside diameter 26.9 mm, inside diameter 21.6 mm) were glued on both ends of the rebars and represent the anchoring. A two-component epoxy glue (GP 49 by Gößl + Pfaff GmbH, Karlskron, Germany) was applied according to the given instruction manual with respect to surface preparations and curing. With greased ball compensation disks and corresponding concave cups, an angle compensation was realized. At the beginning of the experiment, a clip-on extensometer with an initial gauge length (L_{ext}) of 50 mm was attached. A slight load to approx. 2 kN and subsequent relief before the actual start of the test served to minimize any influences caused by alignment effects. The load was controlled by a constant test speed of 1% strain per minute. To protect the measuring instrument, the cylinder was stopped at a tensile force of approx. 100 kN and the extensometer was removed. After that, the experiment was continued until the rod failed. The recorded measurement data includes the test time, the cylinder travel, the cylinder force, and the displacement measurement of the extensometer, all at a frequency of 10 Hz.

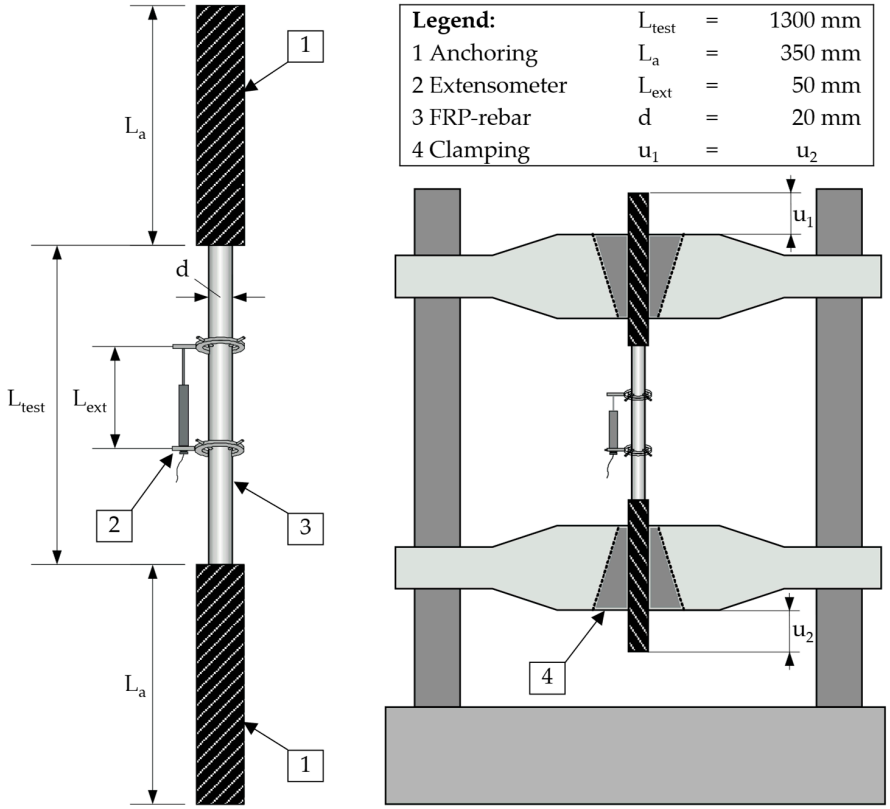

Figure 7. Setup for tensile tests based on ISO 10406-1.

3. Results and Discussion

3.1. DoE Model Quality

The DoE software MODDE® Pro (Version 13.0.2.34314) was used to support the planning and analysis of the trial plan. It connects the planned experiments with the results by means of a mathematical model, which can be used to predict the intended output for a given parameter set. The additional experiments R31 and R32 were also included in the analysis. The software summarizes the model's quality using four parameters, as shown in Table 3, for both the embossing depth and Young's modulus models.

Table 3. Parameters of the model qualities for each intended output (embossing depth and Young's modulus) based on the DoE software MODDE® Pro.

Parameter	Embossing Depth	Young's Modulus
R^2	0.91	0.553
Q^2	0.782	−0.049
Model Validity	0.73	0.9
Reproducibility	0.946	0.326

R^2 represents the coefficient of determination and Q^2 represents the prediction quality. A model with an R^2 value of 0.5 is rather less significant. However, there is no clear distinction between the acceptance and rejection of a model. According to MODDE®, R^2 and Q^2 should not differ by more than 0.3. Similarly, the values for model validity should be >0.25 and reproducibility should be >0.5. The calculated model for embossing depth is considered significant based on these criteria, while the model for Young's modulus is not significant [27]. The insufficient model quality parameters are expected to be attributable to additional factors influencing the Young's modulus, which will be discussed in more detail in Section 3.3.

3.2. Effects on Embossing Depth of the Rebars

Figure 8 summarizes the significant effects on the embossing depth. Haul-off speed is abbreviated as "speed". The larger the effect size, the greater its impact on the target variable in the corresponding direction of the effect. Error bars indicate the respective confidence intervals of the coefficients with a significance level of 95%.

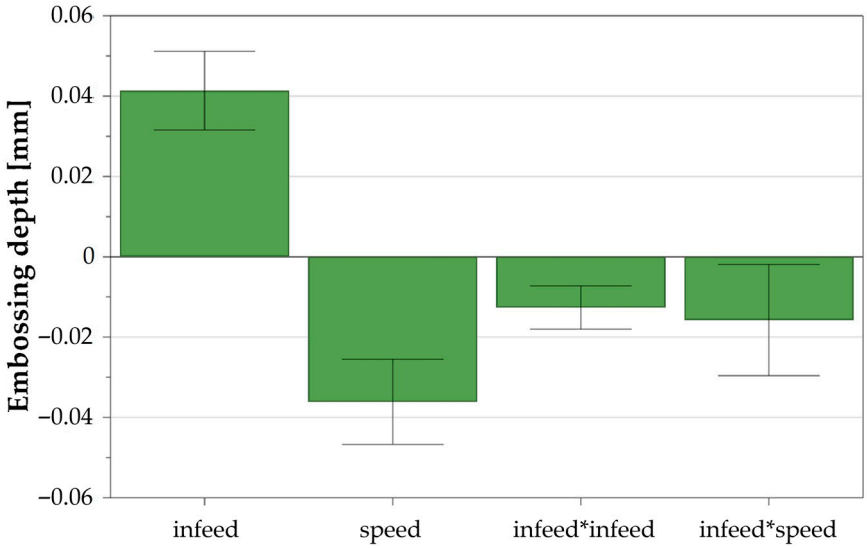

Figure 8. Coefficient diagram for the intended output variable "Embossing depth". The confidence intervals of the scaled and centered coefficients are represented by error bars (95% significance level). Non-significant effects have been removed.

The infeed has a clearly positive linear effect on the embossing depth. Accordingly, the resulting depth increases proportionally with increasing infeed. However, there is also a quadratic negative influence of the infeed. This counteracts the linear increase, albeit in a weaker form, since the absolute value of the quadratic effect is smaller.

There is a negative linear effect on rib height with increased haul-off speed, which is only slightly weaker in terms of its absolute value as the linear effect of the infeed. This means that as the haul-off speed increases, the resulting rib height decreases.

Furthermore, the coefficient diagram shows a negative interaction between the infeed and the haul-off speed. At higher speeds, the positive effect of a larger infeed is less pronounced than at a lower speed. The effect of the infeed is therefore reduced by higher haul-off speeds.

3.2.1. Effect of Infeed

Figure 9 graphically represents the influence of the infeed as the strongest effect on the resulting embossing depth. In addition to the effect curve depending on the set value for the infeed, the 95% confidence interval for the results is also plotted. The almost linearly increasing portion dominates the trend up to an infeed of approximately 1.2 mm. Between an infeed of 1.2 and 1.9 mm, the embossing depth then only increases more slowly until the maximum embossing depth of just under 0.25 mm is reached at an infeed of 1.9 mm. Larger embossing depths are therefore not possible by increasing the infeed alone. However, the decline of the curve as it progresses to higher infeeds is seen as a possible model error and an asymptotic development is more likely to be assumed. The confidence interval widens when the infeed setting exceeds 2 mm, indicating an increasing level of uncertainty in the model.

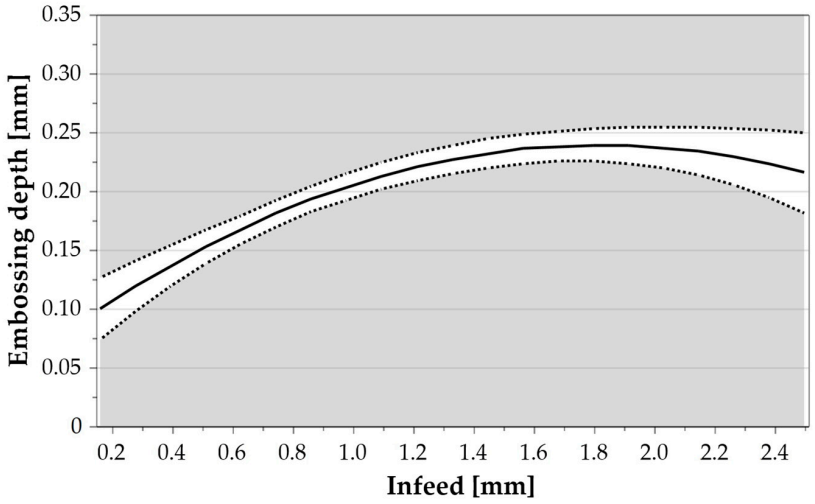

Figure 9. Square effect of the infeed on the embossing depth (solid line). Dotted lines mark the 95% confidence interval.

A plausible explanation is as follows: Increasing infeed raises the strain of the near-surface layers in the embossing contact. For semi-crystalline polyamide 6 at temperatures between T_g and T_m, deformation comprises energy-elastic (crystalline) and entropy-elastic (amorphous) components, with a viscous contribution from chain sliding. We inferred that the delayed entropy-elastic restoring force is consistent with the observed springback, while the viscous component enables permanent deformation [28]. Accordingly, higher infeed increases permanent deformation for a given dwell time. In addition, elastic prestress of fiber bundles contributes a restoring force: As larger infeeds engage deeper fibers, this restoring force likely grows nonlinearly and might contribute to the negative quadratic term in the model. Direct local strain/springback measurements were beyond the present scope and will be addressed in future work.

3.2.2. Effect of Haul-Off Speed

Figure 10 shows the impact of haul-off speed on embossing depth. A linear gradient is observed, with lower embossing depths predicted as haul-off speed increases. At the lowest haul-off speed of 0.3 m/min, the achieved embossing depth is 0.27 mm, while a speed of 1.3 m/min results in a smaller embossing depth of 0.14 mm. Confidence intervals expand at the edges of the observed parameter range.

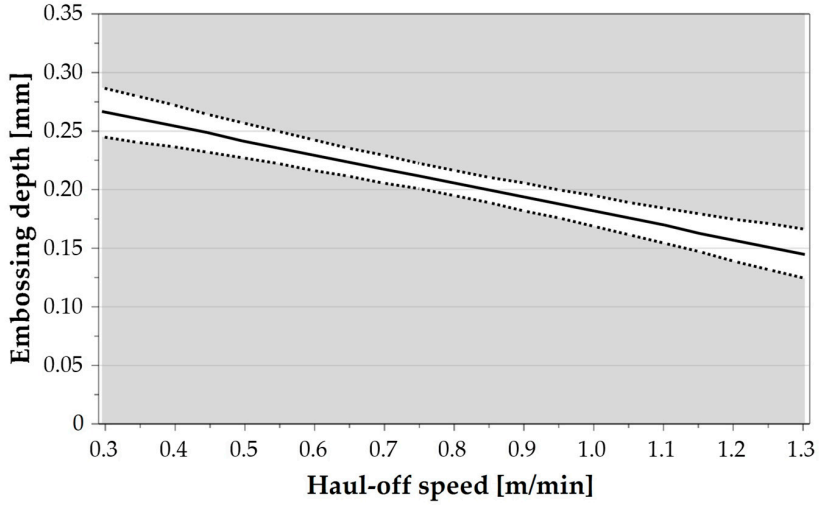

Figure 10. Linear effect of the haul-off speed on the embossing depth (solid line). Dotted lines mark the 95% confidence interval.

We attribute the trend in Figure 10, in part, to temperature-history effects upstream of embossing. At higher haul-off speeds, the time on the air-cooling section is shorter, so the bar reaches the IR zone with a higher through-thickness temperature and greater overall compliance. This favors global cross-sectional deformation and reduces local indentation by the embossing teeth. Conversely, lower haul-off speeds provide longer upstream air-cooling, followed by short IR surface heating to a setpoint, which is expected to steepen the radial temperature gradient and promote more localized surface deformation. Semi-crystalline thermoplastics exhibit strong modulus sensitivity near T_m. Small temperature differences can change shear modulus by orders of magnitude [28], supporting this interpretation. To substantiate the presence of a radial gradient during embossing, we include a first-principles heat-transfer estimate (below). While indicative, these inferences remain to be validated by direct temperature measurements.

To evaluate the presence of a temperature gradient in the bar, radial heat transfer was estimated using Fourier's law for transient heat conduction [29]. Material properties of a glass fiber reinforced polyamide 6 composite (FVF = 40%) are used for this estimation from Reuvers et al., as our own values were not available at the time of writing [30]. The characteristic diffusion time was derived from the thermal diffusivity α, defined as:

$$\alpha = \frac{k}{\rho \cdot c_p}, \tag{1}$$

where k is the thermal conductivity ($0.6365\,\mathrm{W \cdot m^{-1} \cdot K^{-1}}$), ρ is the density ($1800\,\mathrm{kg \cdot m^{-3}}$), and c_p is the specific heat capacity ($1500\,\mathrm{J \cdot kg^{-1} \cdot K^{-1}}$) [30]. For a bar radius $R = 10\,\mathrm{mm} = 0.01\,\mathrm{m}$, the thermal diffusivity becomes:

$$\alpha = 2.36 \cdot 10^{-7}\,\mathrm{m^2 \cdot s^{-1}}, \tag{2}$$

which yields a radial diffusion time of:

$$t = \frac{R^2}{\alpha} \approx 424\,\mathrm{s}. \tag{3}$$

This calculated diffusion time is substantially longer than the brief infrared heating dwell time (between 13 and 56 s in this study), indicating the presence of a pronounced temperature gradient during embossing. This simplified estimate requires validation. Future work will employ embedded micro-thermocouples to directly measure temperature distributions across the rebar radius.

Additionally, at lower speeds, the duration of embossing, which refers to the time during which the embossing force is applied, increases because the rollers rotate at a slower pace. The advantage for the resulting embossing depth is due to the entropy-elastic material behavior of the plastic matrix. As stated in [28], the viscous part of the deformation is time-dependent. Accordingly, with prolonged deformation, more sliding processes can take place between the molecular chains and the permanent part of the deformation increases.

3.2.3. Effect of the Interaction Between Haul-Off Speed and Infeed

Figure 11 shows the interaction between haul-off speed and infeed. At high speeds, the influence of the infeed on the embossing depth is generally small. This can be recognized by the fact that the predicted embossing depths for both the highest and lowest settings of the infeed are close to each other (0.15 mm vs. 0.12 mm). If the haul-off speed is decreased, the beneficial effect of a larger infeed increases significantly compared to a low infeed (0.32 mm vs. 0.19 mm). Therefore, the impact of high infeed settings is most noticeable at low speeds.

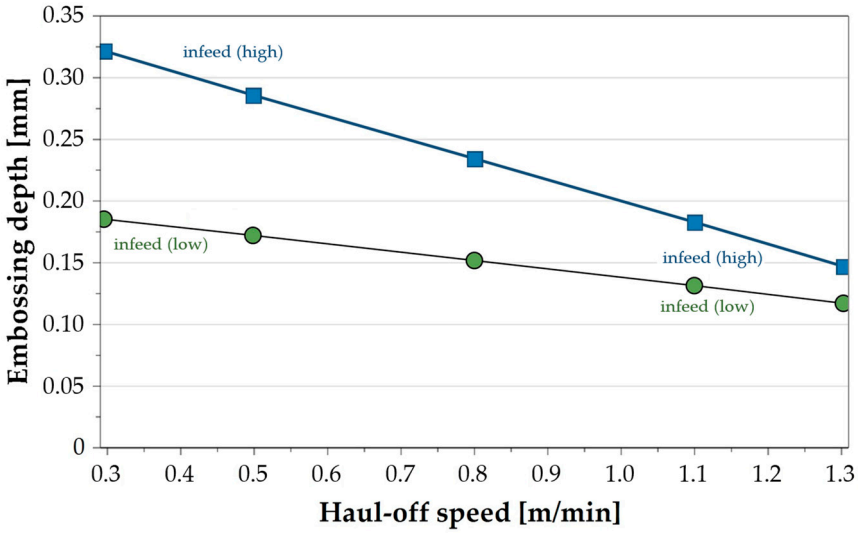

Figure 11. Interaction between the infeed and the haul-off speed. Influence of the haul-off speed on embossing depth with maximum and minimum infeed settings.

One possible explanation for this interaction is a speed-dependent radial temperature distribution created by upstream air cooling followed by short IR surface preheating. At high speeds, limited air-cooling time and shorter IR dwell plausibly yield a shallower gradient and higher overall compliance, so additional infeed primarily increases elastic prestress of deeper fibers, limiting net rib height. At low speeds, longer air-cooling and comparable IR surface heating plausibly steepen the gradient. The cooler core acts as a heat sink that stabilizes the embossed ribs and reduces springback. This interpretation is consistent with the thermal estimate in Section 3.2.2 but has not yet been confirmed by through-thickness temperature measurements.

3.3. Effect on Young's Modulus of the Rebars

Figure 12 shows the mean value and the standard deviation of the Young's modulus from three individual measurements for each test setting of the embossing setup according to the trial plan in Table 1.

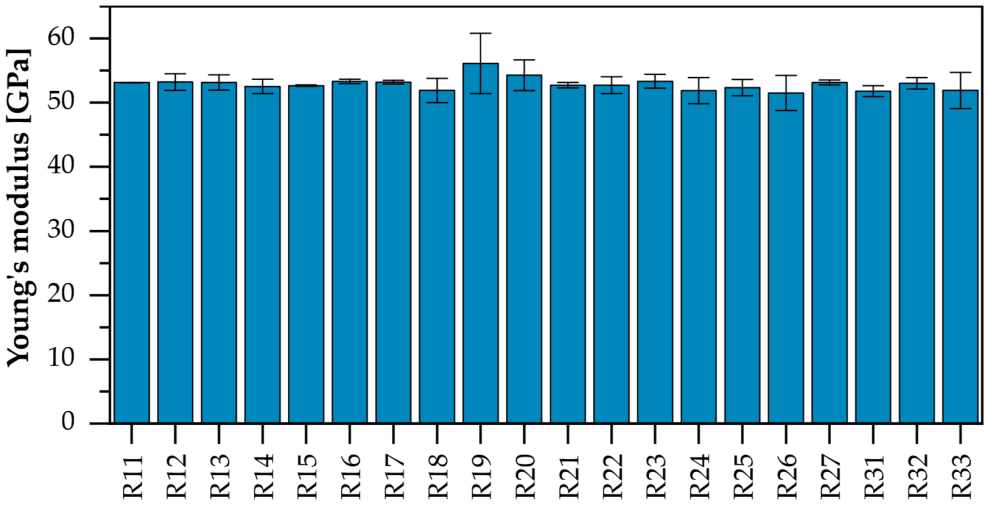

Figure 12. Mean values and standard deviation of the Young's moduli of reinforcing bars manufactured by different process settings. R33 represents smooth bars as reference.

The measured Young's moduli fluctuate around a value of 53 GPa. Compared to other FRP-rebars with a similar FVF of approx. 70% glass fibers, a value close to 60 GPa would be

expected. The small deviation can be attributed to a not yet achieved perfect impregnation quality of the profile core, as the stiffness has been calculated with the nominal diameter of 20 mm. Notably, there are significant variations in spreading widths within certain test groups, such as R19 and R33. Conversely, R11 and R15 exhibit minimal variations. When considering only the mean values, the largest deviation between R19 and R26 is 9%. However, the differences overall are within the low single-digit percentage range.

The possibility of a negative influence caused by the test execution can be practically eliminated. The stress–strain curves utilized are determined within the range of 20 kN to 100 kN, which falls below the typical ultimate tensile forces observed, which are approximately 200 kN. Therefore, linear-elastic material behavior can be assumed in this range. The strain was directly measured on the rod using an extensometer, ensuring that any distortions due to the experimental setup are ruled out.

If the influence of the embossing parameters is considered, no significant effect on the Young's modulus can be detected. An evaluation of the Young's moduli in the context of the DoE method using MODDE® does not yield a significant model, see Table 2. The main reason for this is the large dispersion of the results of the central points compared to the total dispersion (reproducibility = 0.33). A prerequisite for a good model is that the results of repeated experiments are close to each other. The software suggests a minimum of 0.5 as a value for reproducibility. A superposition of several disturbance variables, such as different impregnation qualities of the profile core, could be responsible for the scattering that occurred.

Young's modulus is not the most sensitive metric for detecting surface-layer damage or interlaminar weaknesses. Here it served to verify that inline embossing did not degrade axial stiffness.

3.4. Effects of Embossing on Rebars at the Component Level

This section links the process findings to expected performance at component level by examining near-surface fiber integrity, embossing dwell time and process productivity, and the implications for bond and fiber utilization.

Positioning the embossing device between the die and the pulling unit introduces axial tension in the bar during profiling. Consistent with El-Tahan et al. [12], this tensile prestress helps suppress fiber undulation during forming and thereby limits off-axis waviness in the ribbed surface layer. Longitudinal microsections (Figure 13) show small angular deviations (~5°) from the 0° direction, which, according to Schürmann [31], cause only a minor reduction in axial stiffness. This is in line with the conducted tensile tests (Figure 11), which do not indicate a degradation of Young's modulus relative to smooth reference bars. Moreover, because embossing does not sever near-surface fibers, it avoids the loss of tensile utilization associated with milled grooves [11]. The trade-off is that axial tension and elastic prestress of deeper fiber bundles can increase springback, which partially limits the achievable rib height for a given infeed.

The longitudinal microsection in Figure 13 represents a single section exactly through the bar mid-plane. It shows no fiber damage in the deeper layers and only small near-surface misorientation (~5°). At the same time, the macro image (Figure 6b) reveals localized fiber damage confined to the outermost surface layers, although the precise position along the ribs cannot be unambiguously identified from the macro view. Because the mid-plane section does not intersect those outer regions, localized damage there cannot be excluded. Targeted microsections at rib flanks/roots and multiple circumferential positions are therefore planned.

Beyond axial stiffness, more sensitive tests are required to investigate the ribbed surface layer. Planned characterizations include short-beam interlaminar shear to assess

shear transfer in the near-surface region. This will complement bond tests and help isolate whether observed trends stem from surface-layer shear capacity versus global stiffness.

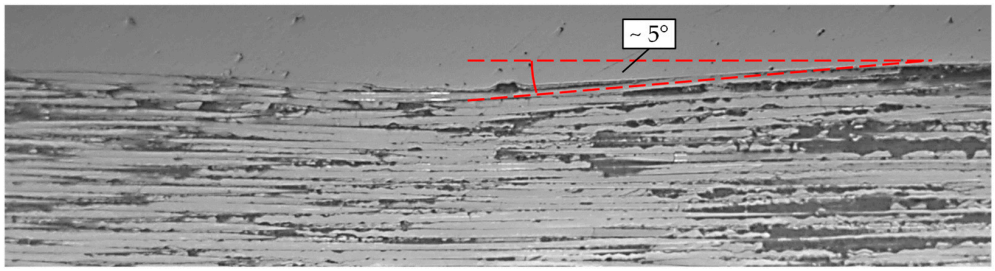

Figure 13. Longitudinal microsection of one embossing from R32. Only small deviations (~5°) from the 0° orientation were observed.

With the two free-rolling embossing rollers used in this study, the embossing time could not be extended to ~5 s suggested in [13]. Nevertheless, the observed increase in rib height at lower haul-off speeds (Figure 10) is consistent with longer force application and a steeper hot-surface/cool-core gradient inferred from the thermal estimate. The time dependence of the viscous deformation component in semi-crystalline aPA6 likely contributes to permanent rib formation during longer effective embossing times. For scale-up, embossing time should be decoupled from line speed, for example, by a driven embossing roller with a larger contact arc or a circumferential press-belt, as conceptually proposed in [13]. Local surface heating and a cool core to limit global cross-sectional flattening should remain.

Regarding bond, the present process achieved rib heights up to 0.38 mm (e.g., R32). Prior studies show that even modest surface deformations (≈0.2 mm) significantly increase bond relative to smooth bars, though the gain is non-linear and failure mechanisms shift with concrete strength [7–9]. In low-strength concretes, concrete rib crushing or winding shear tends to govern, whereas in higher-strength concretes and UHPC, shear of FRP ribs or peeling of surface layers has been observed [7–9]. The embossing concept used in this study preserves fiber continuity at the rib root and aims to raise the shear capacity of the near-surface layer by avoiding fiber cutting, thereby addressing the interlaminar shear-limited bond observed in earlier work. To verify these anticipated benefits quantitatively, dedicated bond testing (e.g., pull-out and beam-end tests) across different concrete strengths is required.

Finally, at the component level, fiber utilization is governed not only by stiffness but also by tensile strength. While no reduction in Young's modulus was detected, future work should determine the tensile utilization rate for embossed bars versus milled alternatives under identical fiber volume fraction and diameter, analogous to the comparison reported by Apitz et al. [11], and correlate it with rib height. Combined with bond tests, this will establish whether embossed thermoplastic FRP rebars simultaneously deliver higher bond efficiency and equal (or better) axial utilization at structural scale.

4. Conclusions

The objective of this study was to investigate FRP rebars that have been manufactured using a newly developed surface profiling method, combined with reactive thermoplastic pultrusion of continuous glass fiber reinforced aPA6. The primary focus was on evaluating the effectiveness of the profiling method. The hot formability of the thermoplastic matrix was utilized to create a ribbed structure through local embossing with minimized damage to near-surface fibers. A temperature gradient with a hotter surface and a cooler core is inferred to be advantageous for embossing, consistent with a radial heat-transfer estimate.

Direct temperature mapping will be used to confirm this in future work. Validation will include pull-out bond tests across different concrete strengths, comparing smooth and embossed bars and reporting bond stress-slip curves. The results show that rib height initially increases linearly with higher infeed but is counteracted by a negative quadratic term, reaching a maximum effect around an infeed of 1.9 mm. The maximum rib height achieved in the test campaign was 0.38 mm at an infeed of 2.5 mm. The significant difference between rib height and infeed is attributed to restoring forces of the profile, influenced by the elastic strain of fibers under tensile stress (springback) and the entropy-elastic behavior of aPA6. A reduction in haul-off speed increases rib height, and an antagonistic interaction between infeed and haul-off speed was observed, where higher speeds reduce the benefit of increased infeed. Tensile tests did not show a significant influence of the embossing method on the Young's modulus of the reinforcing bars.

The microstructural assessment in this study is based on a single longitudinal section through the bar mid-plane. Localized fiber damage observed in macro images appears confined to the outermost surface layers and will be investigated by additional sections in future work. Recognizing that tensile testing is not the most sensitive method for surface-layer assessment, future work will include short-beam interlaminar shear tests, alongside pull-out bond testing, to directly quantify the shear capacity of the ribbed surface layer and its relation to rib geometry.

Author Contributions: Conceptualization, M.F., G.Z. and M.W.; methodology, M.F. and G.Z.; validation, M.F., G.Z. and M.W.; formal analysis, M.F. and G.Z.; investigation, M.F. and G.Z.; resources, F.H.; data curation, M.F. and G.Z.; writing—original draft preparation, M.F., G.Z. and M.W.; writing—review and editing, G.Z., M.W., P.E. and F.H.; visualization, M.F.; supervision, F.H.; project administration, G.Z.; funding acquisition, M.W. and F.H. All authors have read and agreed to the published version of the manuscript.

Funding: This research was funded by the Federal Ministry for Economic Affairs and Climate Action, project "REcyBAR", grant number 03LB2051D.

Data Availability Statement: The original contributions presented in this study are included in the article. Further inquiries can be directed to the corresponding author.

Acknowledgments: The authors would like to thank Johns Manville for the supply of glass fiber rovings. The authors would like to thank RPTU University Kaiserslautern-Landau, especially Tobias Wendler, for the support and access to the tensile testing equipment.

Conflicts of Interest: The authors declare no conflicts of interest.

References

1. WWF Deutschland. *Klimaschutz in der Beton- und Zementindustrie: Hintergrund und Handlungsoptionen*; WWF Deutschland: Berlin, Germany, 2019.
2. Andrew, R.M. Global CO_2 emissions from cement production, 1928–2017. *Earth Syst. Sci. Data* **2018**, *10*, 2213–2239. [CrossRef]
3. Erhard, E.; Weiland, S.; Lorenz, E.; Schladitz, F.; Beckmann, B.; Curbach, M. Anwendungsbeispiele für Textilbetonverstärkung. *Beton- Stahlbetonbau* **2015**, *110*, 74–82. [CrossRef]
4. Estin & Co. *Current Trends in the Global Composites Industry 2021–2026*; JEC Observer: Paris, France, 2022.
5. Benmokrane, B.; Mousa, S.; Mohamed, K.; Sayed-Ahmed, M. Physical, mechanical, and durability characteristics of newly developed thermoplastic GFRP bars for reinforcing concrete structures. *Constr. Build. Mater.* **2021**, *276*, 122200. [CrossRef]
6. Caspari, C. Zur Verbundverankerung von Glasfaserkunststoffbewehrungsstäben in Betonbauteilen unter Kurzzeit- und Langzeitbeanspruchung. Ph.D. Thesis, Technische Universität Kaiserslautern, Kaiserslautern, Germany, 2022.
7. Achillides, Z.; Pilakoutas, K. Bond Behavior of Fiber Reinforced Polymer Bars under Direct Pullout Conditions. *J. Compos. Constr.* **2004**, *8*, 173–181. [CrossRef]
8. Betz, P.; Schumann, A.; Scheerer, S.; Curbach, M. Carbonstäbe im Bauwesen—Teil 5: Einflussfaktoren auf das Verbundverhalten. *Beton- Stahlbetonbau* **2021**, *116*, 924–934. [CrossRef]

9. Hammerl, M.; Stoiber, N.; Hämmerle, J.; Shams, A.; Bischoff, T.; Kromoser, B. Verbundverhalten umwickelter CFK-Stäbe in Beton—Kurzzeituntersuchung der Verbundeigenschaften mittels Pull-out-Tests. *Beton- Stahlbetonbau* **2021**, *116*, 935–946. [CrossRef]
10. Ruiz Emparanza, A.; Kampmann, R.; De Caso y Basalo, F. State-of-the-Practice of Global Manufacturing of FRP Rebar and Specifications. *ACI Fall Conv.* **2017**, *327*, 45.1–45.14. [CrossRef]
11. Apitz, A.; Schmitz, J.; Hückler, A.; Schlaich, M. New thermoplastic carbon fiber reinforced polymer rebars and stirrups. *Struct. Concr.* **2022**, *23*, 923–938. [CrossRef]
12. El-Tahan, M.; Galal, K.; van Hoa, S. New thermoplastic CFRP bendable rebars for reinforcing structural concrete elements. *Compos. Part B Eng.* **2013**, *45*, 1207–1215. [CrossRef]
13. Böhm, R.; Thieme, M.; Wohlfahrt, D.; Wolz, D.; Richter, B.; Jäger, H. Reinforcement Systems for Carbon Concrete Composites Based on Low-Cost Carbon Fibers. *Fibers* **2018**, *6*, 56. [CrossRef]
14. Schumann, A.; May, M.; Schladitz, F.; Scheerer, S.; Curbach, M. Carbonstäbe im Bauwesen. *Beton- Stahlbetonbau* **2020**, *115*, 962–971. [CrossRef]
15. Wang, X.; Peng, Z.; Ding, L.; Lu, J.; Zhu, Z.; Wu, Z. Mechanical and bonding behavior of a bendable fiber-reinforced thermoplastic rebar. *Constr. Build. Mater.* **2021**, *302*, 124222. [CrossRef]
16. Zeng, J.-J.; Sun, H.-Q.; Xia, J.-R.; Feng, S.-Z.; Zhao, B.; Zhou, J.-K.; Zhuge, Y. Bond behavior between concrete and thermoplastic GFRP bars with novel surface features. *Eng. Struct.* **2025**, *343*, 121161. [CrossRef]
17. Clark, J.C.; Davids, W.G.; Lopez-Anido, R.A.; Schanck, A.P.; Sheltra, C.A. Continuously Formed Fiber-Reinforced Thermoplastic Composite Rebar for Concrete Reinforcement. *J. Compos. Sci.* **2025**, *9*, 378. [CrossRef]
18. Luo, Y.; Lin, G.; Chen, J.-F.; Wu, J. Thermoplastic fiber-reinforced polymer composites in construction: A state-of-the-art review. *Case Stud. Constr. Mater.* **2025**, *23*, e05596. [CrossRef]
19. Zeng, J.-J.; Feng, S.-Z.; Zhao, B.; Wu, F.-Y.; Zhuge, Y.; Wang, H. Recyclable thermoplastic FRP bars for reinforced concrete structures: Current status and future opportunities. *Compos. Struct.* **2024**, *348*, 118438. [CrossRef]
20. van Rijswijk, K.; Bersee, H. Reactive processing of textile fiber-reinforced thermoplastic composites—An overview. *Compos. Part A Appl. Sci. Manuf.* **2007**, *38*, 666–681. [CrossRef]
21. Wilhelm, M.L. *Verfahrensentwicklung für die Herstellung Kontinuierlich Faserverstärkter, Thermoplastischer Profile im Pultrusionsverfahren Mittels In-Situ Polymerisation von ε-Caprolactam*; Fraunhofer Verlag: Stuttgart, Germany, 2025.
22. Wilhelm, M.L.; Zeeb, G.; Rosenberg, P.; Henning, F. In-situ pultrusion of nylon 6 based profiles—Key parameters of the process. In Proceedings of the CAMX 2023, Atlanta, GA, USA, 30 October–2 November 2023; NA SAMPE. [CrossRef]
23. Fowlkes, W.Y.; Creveling, C.M. *Engineering Methods for Robust Product Design: Using Taguchi Methods in Technology and Product Development*, 1st ed.; Addison-Wesley: Reading, MA, USA, 1995; ISBN 0201633671.
24. Niewels, J. Zum Tragverhalten von Betonbauteilen mit Faserverbundkunststoff-Bewehrung. Ph.D. Thesis, Rheinisch-Westfälischen Technische Hochschule Aachen, Aachen, Germany, 2008.
25. Cho, B.-G.; McCarthy, S.P.; Fanucci, J.P.; Nolet, S.C. Fiber reinforced nylon-6 composites produced by the reaction injection pultrusion process. *Polym. Compos.* **1996**, *17*, 673–681. [CrossRef]
26. *ISO 10406-1*; Fibre-Reinforced Polymer (FRP) Reinforcement of Concrete—Test Methods: Part 1: FRP Bars and Grids. ISO: Geneva, Switzerland, 2025.
27. *MODDE© Pro*, Version 13.0.2.34314; Sartorius Stedim Data Analytics AB: Umeå, Sweden, 2021.
28. Eyerer, P.; Hirth, T.; Elsner, P. *Polymer Engineering*; Springer: Berlin/Heidelberg, Germany, 2008; ISBN 978-3-540-72402-5.
29. Lienhard V, J.H.; Lienhard, J.H., IV. *A Heat Transfer Textbook*, 6th ed.; Phlogiston Press: Cambridge, MA, USA, 2024.
30. Reuvers, M.-C.; Dannenberg, C.; Kulkarni, S.; Loos, K.; Johlitz, M.; Lion, A.; Reese, S.; Brepols, T. Experimental investigation and micromechanical analysis of glass fiber reinforced polyamide 6. *Mech. Mater.* **2024**, *199*, 105144. [CrossRef]
31. Schürmann, H. *Konstruieren mit Faser-Kunststoff-Verbunden*; 2., Bearb. und Erw. Aufl.; Springer: Berlin/Heidelberg, Germany, 2007; ISBN 978-3-540-72189-5.